Composites: Part A 199 (2025) 109162

Contents lists available at ScienceDirect

Composites Part A

journal homepage: www.elsevier.com/locate/compositesa

3D solid-shell element for macroscopic composite forming simulation enabling thickness prediction

Bastian Schäfer *, Johannes Mitsch, Luise Kärger *

Lightweight Engineering, Institute of Vehicle System Technology (FAST), Karlsruhe Institute of Technology (KIT), Karlsruhe, 76131, Germany

ARTICLE INFO

Keywords:
Solid-shell
Finite element analysis
Non-crimp fabric
Process simulation
Forming simulation
Preforming

ABSTRACT

Accurate finite element (FE) forming simulations of engineering textiles are essential for optimizing manufacturing processes such as liquid composite molding (LCM). Traditional two-dimensional approaches often neglect through-thickness compaction, which is essential for predicting fiber volume content and final part thickness. This study presents an advanced reduced-integrated 8-node hexahedral solid-shell element designed specifically for macroscopic forming simulations of engineering textiles. The proposed element incorporates methods to prevent numerical locking, a membrane-bending decoupling method and a novel hourglass stabilization technique to ensure numerical efficiency. The solid-shell is implemented as a user-defined element (VUEL) in ABAQUS/EXPLICIT and applied to a bidirectional non-crimp fabric (NCF). It is parameterized based on experimental bias-extension, plate-to-plate compaction, and cantilever bending tests. Application to hemispherical forming simulations validates its forming behavior, achieving comparable accuracy to conventional 2D methods with the additional advantage of predicting thickness changes. In conclusion, this work provides a three-dimensional modeling approach that enhances process simulation capabilities for composite preforming, enabling more accurate predictions of effects in thickness direction.

1. Introduction

Finite element (FE) forming simulations can be applied to investigate and optimize manufacturing processes such as the preforming step of liquid composite molding (LCM) for continuously fiber-reinforced polymers from engineering textiles. Therefore, the main deformation modes of textiles, comprising the in-plane membrane, out-of-plane bending as well as through-thickness compaction behavior, must be modeled to accurately predict forming effects and defects [1]. The majority of macroscopic textile forming simulations are based on two-dimensional finite elements with a plane-stress assumption and focus on the membrane and bending behavior to efficiently predict the final fiber orientation, preform shape as well as out-of-plane wrinkling [2–4]. However, these approaches neglect the compaction behavior, which determines a layer's thickness as well as fiber volume content and consequently influences the permeability, necessary press forces as well as resulting mechanical properties of components. A three-dimensional (3D) approach with compaction is especially necessary for modeling LCM processes involving fluid–structure interaction, such as wet compression modeling, as demonstrated by Poppe et al. [5].

Compaction during forming is often investigated based on mesoscopic approaches [6–9] or by isolated macroscopic simulations of critical corners for single-curved geometries with multiple conventional 3D elements ever the thickness [10]. The modeling of compaction in macroscopic forming simulations requires a suitable 3D element formulation, which introduces two distinct challenges: the necessity for a membrane-bending decoupling and for preventing numerical locking of low-order elements.

Membrane-bending decoupling. Engineering textiles have a high tensile stiffness in fiber direction due to the quasi-inextensible fibers. In contrast, the typically low friction between fibers allows relative movement under bending and results in a low bending stiffness. This behavior cannot be modeled with conventional shell theories and therefore membrane and bending behavior is usually considered in a decoupled fashion in macroscopic forming simulations [3,11]. For 2D elements, an intrinsic decoupling can be accomplished within a single element by specific shell approaches [12–15] or a variable stiffness over the thickness [16,17]. An extrinsic decoupling can be accomplished by superimposing membrane and shell elements [18–20]. For 3D elements, generalized continua approaches can be applied for textile forming simulations [21,22], based on higher-grade or higher-order continuum theories [23, pp. 686–691]. However, this requires specialized element formulations [24,25] or specific solvers [26,27] with access to information based on neighboring elements. They have been exclusively

* Corresponding authors.
E-mail addresses: bastian.schaefer@kit.edu (B. Schäfer), luise.kaerger@kit.edu (L. Kärger).

https://doi.org/10.1016/j.compositesa.2025.109162
Received 14 April 2025; Received in revised form 30 June 2025; Accepted 4 July 2025
Available online 15 July 2025

applied for thick interlock woven composites [21,28], which do not require a complete decoupling of membrane and bending behavior. In addition, the high transverse shear stiffness and high thickness of thick interlock fabrics reduces the impact of numerical locking.

Numerical locking. The term *locking* describes the occurrence of purely numerically caused parasitic stresses, if the element formulation cannot represent a specific deformation mode and the predicted behavior is too stiff [23, pp. 584–598]. The relevant phenomena during forming of initially flat textiles are membrane, (transverse) shear and Poisson locking [29–31].

Different methods to prevent locking are described in literature. First, *increasing the polynomial order* of the shape functions alleviates locking by increasing the capabilities of the element to comply with deformation modes [31, p. 258]. However, this significantly increases the numerical effort and is rarely applied for explicit integration schemes commonly utilized for forming simulations. Second, *selected reduced integration schemes (SRI)* can be used to strategically position integration points at locations with zero parasitic stresses for a particular component [32]. SRI is computationally very efficient, but requires specific stabilization procedures to prevent hourglassing. Third, the *assumed natural strain method (ANS)* can help reduce locking by separating the strain tensor into locking and locking-free parts [33]. A re-interpolation of specific strain components is applied based on collocation points at known zero points of the specific parasitic stresses. Fourth, the *enhanced assumed strain (EAS) method* or alternatively incompatible mode elements, introduces additional internal strain degrees of freedom (DOF) α_e to capture more deformation modes [34].

Solid-shells. Solid-shell elements are 3D elements with a predefined thickness direction that combine the above outlined methods to prevent locking, especially in thin structures under bending. Unlike classical shell elements, they use general 3D material models, have only translational DOFs, and facilitate contact modeling without extra kinematic assumptions. Various formulations of solid-shell elements have been proposed in literature, which are compared to each other in different studies [35–38], with only a small overview in the following. The main distinguishing features are the integration scheme, the number of collocation points for the ANS and the number of EAS-DOF.

Hauptmann and co-authors introduced the first fully integrated solid-shell formulations for implicit [39–41] and later explicit [42,43] time integration schemes in structural applications. Similar solid-shell elements were developed by Vu-Quoc and Tan for simulations of multilayered composites [44–46]. Reduced-integrated formulations are numerically more efficient and inherently less prone to locking due to the location of integration points, but require material-specific hourglass stabilization. Reese et al. [47,48] proposed the first solid-shell with a single integration point and three EAS-DOF. This concept was extended by Sousa et al. [49,50] to SRI with a variable number of integration points in thickness direction and applied to sheet metal forming simulations [51,52].

Schwarze and Reese [36,37] proposed a solid-shell element denoted as Q1STs with SRI, four-point ANS and a single EAS-DOF, which was later extended to an explicit formulation by Pagani et al. [53]. They directly compared their element's performance to previous approaches [44,49,52] and found an increased performance in particular for very high slenderness. The Q1STs element showed promising results for structural simulations of fiber-reinforced composites [54,55], deep drawing of sheet metals [53,56] as well as packaging simulation of anisotropic cardboard [57].

Alternative solid-shell formulations introduce additional nodes with global DOFs instead of EAS-DOF to improve the modeling of pinching stresses and Neumann boundary conditions. For instance, Dia et al. [58] proposed a nine-node hexahedral solid-shell formulation with an additional translational DOF in the center. The formulation produced promising results in standard shell element tests and when applied to the forming of an isotropic material with hardening. However, the implementation of additional global DOFs requires specific solvers, and these formulations have not been applied to the forming of anisotropic materials or enhanced by membrane-bending decoupling.

3D approaches for composite forming. Chen et al. [59,60] outlined an 8-node solid-shell concept for thermoforming of a thermoplastic woven with decoupled contributions for membrane, bending and compression. Plausible results are obtained for the shear angle distribution and interply slippage for closed tools. However, no methods to prevent locking or validations of the out-of plane deformation are presented.

Xiong et al. [61,62] proposed a 6-node and a 7-node prismatic element to investigate consolidation of thermoplastic tapes after forming. The 6-node formulation combines a constant strain triangle formulation for the membrane part with a Kirchhoff plate theory with zero transverse shear strains for the bending part. The 7-node formulation introduces an additional node in the element center with a single global DOF to enable the use of a fully 3D constitutive law and improve pinching stress prediction. Both formulations perform well in different classical tests for shell elements with isotropic material behavior [61]. In addition, plausible thermoforming results are achieved with the 7-node element for again closed tools and subsequent consolidation [61,62]. However, it requires a global DOF compared to an internal EAS-DOF, which limits the implementation to specific solvers.

Poppe et al. [5,63] superimposed a built-in prismatic continuum shell (SC6R) for the textile deformation with a user-defined element VUEL in ABAQUS/EXPLICIT for fluid propagation to model fluid–structure interaction during wet compression molding. The built-in continuum shell cannot model a membrane-bending decoupling. Thus, the low bending stiffness of the textile is modeled by reducing the transverse shear stiffness instead of a decoupling. This enables an acceptable approximation for the out-of plane behavior, but limits the approach to an isotropic bending behavior with a constant bending stiffness. In addition, the continuum shell can only model a constant compaction stiffness. Thus, the non-linear compaction behavior of the textile is modeled in the superimposed fluid VUEL instead. Poppe et al. [5,63] achieved a good prediction of the textile and fluid behavior during the forming process by the superimposed approach, but due to the limitations of the built-in continuum shell, it cannot be extended to more complex material behavior.

Scope of this work. Solid-shell elements are a promising option for modeling forming and simultaneous compaction, but a locking-free formulation without limitations on the material model and with a membrane-bending decoupling for composite forming has not yet been presented. In this work, a solid-shell element for textile forming with an intrinsic membrane-bending decoupling within a single element and verified locking-free bending behavior is proposed. It is an 8-node hexahedral solid-shell element with only translational degrees of freedom, based on the Q1STs formulation proposed by Schwarze and Reese [36,37]. The element is implemented as a user-defined element VUEL in the commercial solver ABAQUS/EXPLICIT. This work builds on preliminary investigations performed for generic isotropic [64] and highly anisotropic [65] materials. The commercially available solid elements in Abaqus/Explicit exhibited locking effects for pronounced anisotropy, rendering them ill-suited for application in textile forming processes. In comparison, the locking-free bending behavior of the proposed solid-shell in forming simulations is verified by comparison to various shell and solid elements [64,65]. In this work, an approach for the membrane-bending decoupling in combination with an hourglass stabilization is proposed, based on a Taylor approximation of the Green–Lagrange strain around the out-of-plane direction. The goal is to represent each textile layer with a single element layer to limit the computational effort and ensure direct transferability of methods developed for 2D approaches. The solid-shell is applied to macroscopic forming simulations of a symmetrical 0°/90° bidirectional non-crimp fabric and validated with experimental forming tests.

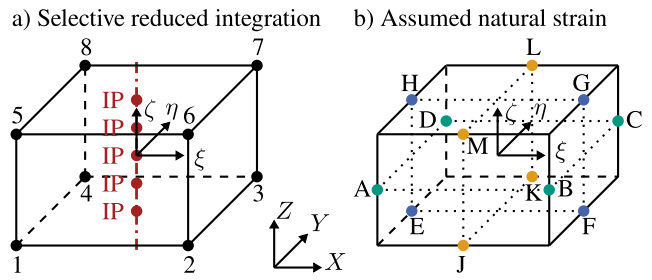

Fig. 1. Isoparametric solid-shell element | (a) Conventions for the element nodes 1-8 and integration points (IP), (b) Collocation points for the ANS method [64].

2. Solid-shell formulation

2.1. Fundamental element formulation

The solid-shell formulation is based on the Q1STs element proposed by Schwarze and Reese [36,37] with the adaptations form Pagani et al. [53] for explicit time integration. A comprehensive overview of the formulation can be found in the original work. The following section delineates the key aspects that are pertinent to the adaptations to textile forming.

The solid-shell is derived from an isoparametric 8-node hexahedral brick-element with trilinear shape functions [23, pp. 188–190]. It applies the two-field form of the Hu–Washizu variational principle proposed by Simo and Rifai [34]

$$\delta g_1(\boldsymbol{u},\boldsymbol{\alpha}) = \int_{V_0} \boldsymbol{S}(\boldsymbol{E}) : \delta \boldsymbol{E}_\mathrm{c} \mathrm{d}V + \int_{V_0} \rho \ddot{\boldsymbol{u}} \cdot \delta \boldsymbol{u} \mathrm{d}V - \delta g^\mathrm{ext} = 0 \tag{1}$$

in combination with the orthogonality condition

$$\delta g_2(\boldsymbol{u},\boldsymbol{\alpha}) = \int_{V_0} \boldsymbol{S}(\boldsymbol{E}) : \delta \boldsymbol{E}_\mathrm{e} \mathrm{d}V = 0, \tag{2}$$

where ρ is the material density, V is the volume, δg^ext is the virtual work of external loads and $\boldsymbol{S}(\boldsymbol{E})$ is the second Piola–Kirchhoff stress depending on the total Green–Lagrange strain. The strain is additively split according to the EAS method [34]

$$\boldsymbol{E} = \boldsymbol{E}_\mathrm{c}(\boldsymbol{u}) + \boldsymbol{E}_\mathrm{e}(\alpha_\mathrm{e}) \tag{3}$$

into a compatible part $\boldsymbol{E}_\mathrm{c}$ depending solely on the displacements $\boldsymbol{u}$, and an enhanced part $\boldsymbol{E}_\mathrm{e}$ depending for the chosen element formulation on a single additional enhanced DOF α_e. The material coordinates $\boldsymbol{X}$ and displacement $\boldsymbol{u}$ in isoparametric coordinates $\boldsymbol{\xi}$ ($\xi_1 = \xi$, $\xi_2 = \eta$ and $\xi_3 = \zeta$) are calculated from

$$\boldsymbol{X}(\boldsymbol{\xi}) = \sum_{I=1}^{8} N_I \boldsymbol{X}_I^\mathrm{node} \quad \text{and} \quad \boldsymbol{u}(\boldsymbol{\xi}) = \sum_{I=1}^{8} N_I \boldsymbol{u}_I^\mathrm{node} \tag{4}$$

$$\text{with} \quad N_I = \frac{1}{8}(1+\xi_I\xi)(1+\eta_I\eta)(1+\zeta_I\zeta), \tag{5}$$

where index I refers to the nodes, shown in Fig. 1a.

A *selective reduced integration scheme (SRI)* is applied with full integration along the thickness direction and variable number of integration points along $\boldsymbol{\xi}^\star \hat{=} \{0,0,\zeta\}^\mathsf{T}$, cf. Fig. 1a. Reduced in-plane integration prevents in-plane shear locking. Pagani et al. [53] demonstrated the efficiency and suitability of this approach to describe nonlinear behavior in the thickness direction for explicit simulations.

The *assumed natural strain method (ANS)* is applied to the compatible strain in the isoparametric domain $\bar{\boldsymbol{E}}_\mathrm{c}$. It is based on four collocation points $P_{\xi_i\xi_j}$ to prevent locking and increase stability in the reduced integrated element compared to two-point ANS [52]. The locations of the collocation points are shown in Fig. 1b. ANS is applied to the transverse normal component $E_{\mathrm{c},\zeta\zeta}$ based on Betsch and Stein [66] to prevent curvature-thickness locking ($P_{\zeta\zeta} \in \{\mathrm{A,B,C,D}\}$). ANS is applied to the transverse shear components $E_{\mathrm{c},\eta\zeta}$ ($P_{\eta\zeta} \in \{\mathrm{E,F,G,H}\}$) and $E_{\mathrm{c},\xi\zeta}$ ($P_{\xi\zeta} \in \{\mathrm{J,K,L,M}\}$) based on Bathe and Dvorkin [33] to prevent transverse shear locking. This results in

$$\bar{E}^\mathrm{ANS}_{\mathrm{c}\zeta\zeta}(\xi,\eta) = \sum_{P_{\xi\zeta}=\mathrm{A}}^{\mathrm{D}} \frac{1}{4}(1+\xi_{P_{\zeta\zeta}}\xi)(1+\eta_{P_{\zeta\zeta}}\eta)\bar{E}_{\mathrm{c},\zeta\zeta}\left(\boldsymbol{\xi}_{P_{\zeta\zeta}}\right), \tag{6}$$

$$\bar{E}^\mathrm{ANS}_{\mathrm{c}\eta\zeta}(\xi,\zeta) = \sum_{P_{\eta\zeta}=\mathrm{E}}^{\mathrm{H}} \frac{1}{4}(1+\xi_{P_{\eta\zeta}}\xi)(1+\zeta_{P_{\eta\zeta}}\zeta)\bar{E}_{\mathrm{c},\eta\zeta}\left(\boldsymbol{\xi}_{P_{\eta\zeta}}\right), \tag{7}$$

$$\bar{E}^\mathrm{ANS}_{\mathrm{c}\xi\zeta}(\eta,\zeta) = \sum_{P_{\xi\zeta}=\mathrm{J}}^{\mathrm{M}} \frac{1}{4}(1+\eta_{P_{\xi\zeta}}\eta)(1+\zeta_{P_{\xi\zeta}}\zeta)\bar{E}_{\mathrm{c},\xi\zeta}\left(\boldsymbol{\xi}_{P_{\xi\zeta}}\right). \tag{8}$$

The *enhanced assumed strain method (EAS)* is applied to prevent volumetric locking. Because ANS results in a constant transverse normal component $\bar{E}^\mathrm{ANS}_{\mathrm{c}\zeta\zeta}$, the enhanced strain tensor $\boldsymbol{E}_\mathrm{e}$ is constructed to introduce a linear component in the isoparametric domain ($\bar{\bullet}$) with a single enhanced DOF α_e. In Voigt matrix notation ($\hat{\bullet}$) this results in

$$\hat{\bar{\boldsymbol{E}}}_\mathrm{e} = \hat{\bar{\boldsymbol{B}}}_\mathrm{e}\alpha_\mathrm{e} \quad \text{with} \quad \hat{\bar{\boldsymbol{B}}}_\mathrm{e} \hat{=} [0,0,\zeta,0,0,0]^\mathsf{T}. \tag{9}$$

The main advantage of this simple EAS formulation as demonstrated by Pagani et al. [53], is the estimation of α_e within a single iteration of an explicit dynamic integration scheme, due to the small time step size.

For hourglass stabilization, a *Taylor expansion of the compatible strain* around the element center $\boldsymbol{\xi}^0 = \boldsymbol{0}$ is carried out

$$\hat{\boldsymbol{E}}_\mathrm{c} \approx \underbrace{\hat{\boldsymbol{E}}_\mathrm{c}^0 + \zeta\hat{\boldsymbol{E}}_\mathrm{c}^\zeta + \zeta^2\hat{\boldsymbol{E}}_\mathrm{c}^{\zeta\zeta}}_{\hat{\boldsymbol{E}}_\mathrm{c}^\star} + \underbrace{\xi\hat{\boldsymbol{E}}_\mathrm{c}^\xi + \eta\hat{\boldsymbol{E}}_\mathrm{c}^\eta + \xi\eta\hat{\boldsymbol{E}}_\mathrm{c}^{\xi\eta} + \eta\zeta\hat{\boldsymbol{E}}_\mathrm{c}^{\eta\zeta} + \xi\zeta\hat{\boldsymbol{E}}_\mathrm{c}^{\xi\zeta}}_{\hat{\boldsymbol{E}}_\mathrm{c}^\mathrm{hg}} \tag{10}$$

to separate a part $\hat{\boldsymbol{E}}_\mathrm{c}^\star$ related to the full integration in thickness direction and a part $\hat{\boldsymbol{E}}_\mathrm{c}^\mathrm{hg}$ unaffected by the SRI. Thereby, $\hat{\boldsymbol{E}}_\mathrm{c}^{\xi_i} = \left.\dfrac{\partial \hat{\boldsymbol{E}}_\mathrm{c}}{\partial \xi_i}\right|_{\boldsymbol{\xi}=\boldsymbol{\xi}^0}$ are constant matrices, detailed in [37]. The strain part $\hat{\boldsymbol{E}}_\mathrm{c}^\mathrm{hg}$ is essential for an hourglass stabilization to achieve a full rank of the element stiffness matrix despite the reduced in-plane integration. A similar Taylor expansion of the stress around the normal through the center $\boldsymbol{\xi}^\star$ is carried out

$$\hat{\boldsymbol{S}} \approx \underbrace{\hat{\boldsymbol{S}}\left(\hat{\boldsymbol{E}}^\star\right)}_{\hat{\boldsymbol{S}}^\star} + \underbrace{\overbrace{\left.\frac{\partial \hat{\boldsymbol{S}}(\hat{\boldsymbol{E}})}{\partial \hat{\boldsymbol{E}}}\right|_{\boldsymbol{\xi}=\boldsymbol{\xi}^\star}}^{\hat{\mathbb{C}}^\star} : \left(\xi\hat{\boldsymbol{E}}_\mathrm{c}^\xi + \eta\hat{\boldsymbol{E}}_\mathrm{c}^\eta + \xi\zeta\hat{\boldsymbol{E}}_\mathrm{c}^{\xi\zeta} + \eta\zeta\hat{\boldsymbol{E}}_\mathrm{c}^{\eta\zeta}\right)}_{\hat{\boldsymbol{S}}^\mathrm{hg}} \tag{11}$$

to separate a part related to the full integration in thickness direction $\hat{\boldsymbol{S}}^\star$ and hourglass stabilization $\hat{\boldsymbol{S}}^\mathrm{hg}$. The material stiffness tangent $\hat{\mathbb{C}}^\star$ can be material- and deformation-dependent in thickness direction. To enable an efficient analytical integration of the hourglassing terms while maintaining full rank, it is approximated by a constant material tangent $\hat{\mathbb{C}}^\mathrm{hg}$ [37]. The Taylor expansion of the strain and stress are necessary for the hourglass stabilization due to the SRI and enable later adaptations for engineering textiles, cf. Section 2.2.

Finally, the *discretization and integration* of Eqs. (1) and (2) is carried out on element level. The element volume is approximated with the Jacobian at the center by

$$\mathrm{d}V^\mathrm{e} = \det \boldsymbol{J}|_{\boldsymbol{\xi}=\boldsymbol{\xi}^0} \mathrm{d}\Omega^\mathrm{e} = \boldsymbol{J}^0 \mathrm{d}\xi\mathrm{d}\eta\mathrm{d}\zeta. \tag{12}$$

In combination with Eqs. (9)–(11), the discretized weak element formulation of Eqs. (1) and (2) results in

$$\boldsymbol{G}_1 = \boldsymbol{R}_\mathrm{u}^\star + \boldsymbol{R}_\mathrm{u}^\mathrm{hg} + \boldsymbol{M}\ddot{\boldsymbol{u}} - \boldsymbol{G}_\mathrm{ext} = \boldsymbol{0} \quad \text{and} \tag{13}$$

$$G_2 = R_\alpha^\star = 4\boldsymbol{J}^0 \int_{-1}^{1} \hat{\boldsymbol{B}}_\mathrm{e}^\mathsf{T} \cdot \hat{\boldsymbol{S}}^\star \mathrm{d}\zeta = 0, \tag{14}$$

where $\boldsymbol{M}$ is the element mass matrix and $\boldsymbol{G}_\mathrm{ext}$ the external element force vector. The internal forces related to the out-of-plane integration $\boldsymbol{R}_\mathrm{u}^\star$

and hourglass-stabilized volume integration $\boldsymbol{R}_{\mathrm{u}}^{\mathrm{hg}}$ are derived as

$$\begin{aligned}\boldsymbol{R}_{\mathrm{u}}^{\star} &= \int_{\Omega^{\mathrm{e}}} \hat{\boldsymbol{B}}_{\mathrm{c}}^{\star\mathsf{T}} \cdot \hat{\boldsymbol{S}}^{\star} J^0 \mathrm{d}\Omega^{\mathrm{e}} \\ &= 4J^0 \int_{-1}^{1} \left(\hat{\boldsymbol{B}}_{\mathrm{c}}{}^{0} + \zeta \hat{\boldsymbol{B}}_{\mathrm{c}}{}^{\zeta} + \zeta^2 \hat{\boldsymbol{B}}_{\mathrm{c}}{}^{\zeta\zeta}\right)^{\mathsf{T}} \cdot \hat{\boldsymbol{S}}^{\star} \mathrm{d}\zeta, \end{aligned} \tag{15}$$

$$\begin{aligned}\boldsymbol{R}_{\mathrm{u}}^{\mathrm{hg}} &= \int_{\Omega^{\mathrm{e}}} \hat{\boldsymbol{B}}_{\mathrm{c}}{}^{\mathrm{hg}\mathsf{T}} \cdot \hat{\boldsymbol{S}}^{\mathrm{hg}} J^0 \mathrm{d}\Omega^{\mathrm{e}} \\ &= \frac{8}{3} J^0 \left(\hat{\boldsymbol{B}}_{\mathrm{c}}{}^{\xi\mathsf{T}} \cdot \left(\hat{\mathbb{C}}^{\mathrm{hg}} : \hat{\boldsymbol{E}}_{\mathrm{c}}{}^{\xi}\right) + \hat{\boldsymbol{B}}_{\mathrm{c}}{}^{\eta\mathsf{T}} \cdot \left(\hat{\mathbb{C}}^{\mathrm{hg}} : \hat{\boldsymbol{E}}_{\mathrm{c}}{}^{\eta}\right)\right) \\ &+ \frac{8}{9} J^0 \left(\hat{\boldsymbol{B}}_{\mathrm{c}}{}^{\eta\zeta\mathsf{T}} \cdot \left(\hat{\mathbb{C}}^{\mathrm{hg}} : \hat{\boldsymbol{E}}_{\mathrm{c}}{}^{\eta\zeta}\right) + \hat{\boldsymbol{B}}_{\mathrm{c}}{}^{\xi\zeta\mathsf{T}} \cdot \left(\hat{\mathbb{C}}^{\mathrm{hg}} : \hat{\boldsymbol{E}}_{\mathrm{c}}{}^{\xi\zeta}\right)\right) \end{aligned} \tag{16}$$

Thereby, $\hat{\boldsymbol{B}}_{\mathrm{c}}^{(\bullet)}$ are constant operator matrices representing the relation between the respective virtual compatible strains $\delta\hat{\boldsymbol{E}}_{\mathrm{c}}^{(\bullet)}$ and displacements according to $\delta\hat{\boldsymbol{E}}_{\mathrm{c}}^{(\bullet)} = \hat{\boldsymbol{B}}_{\mathrm{c}}^{(\bullet)} \cdot \delta\boldsymbol{u}$, detailed in [37]. The discretized weak form of the orthogonality condition G_2 in Eq. (14) is used to iteratively update the EAS-DOF α_{e} based on static condensation at the element level as proposed by Simo et al. [67]. An explicit estimate of $\Delta\alpha_{\mathrm{e}}$ is calculated by linearization with respect to α_{e}

$$\Delta\alpha_{\mathrm{e}} = -S_{\alpha\alpha}^{-1} R_{\alpha}^{\star} \quad \text{with} \quad S_{\alpha\alpha} = 4J^0 \int_{-1}^{1} \hat{\boldsymbol{B}}_{\mathrm{e}}^{\star\mathsf{T}} \cdot \left(\hat{\mathbb{C}}^{\star} : \hat{\boldsymbol{B}}_{\mathrm{e}}^{\star}\right) \mathrm{d}\zeta. \tag{17}$$

An accurate approximation is achieved with a single iteration in explicit time integration due to the small time step size, as demonstrated by Pagani et al. [53].

2.2. Modification for forming of engineering textiles

The locking-free behavior of the Q1STs solid-shell element, outlined Section 2.1, has been shown by Schwarze and Reese for small [36] and large [37] deformations in several well-known benchmarks [68]. It was also applied to structural simulations of consolidated fiber-reinforced composites [54,55], deep drawing of sheet metals [53,56] and packaging simulation of cardboard [57]. In our previous investigations, it outperformed conventional shell and solid elements available in Abaqus for forming generic isotropic [64] and highly anisotropic [65] materials by accurately predicting in-plane and out-of-plane deformation. However, some modifications are necessary to adapt it for forming simulations of engineering textiles.

First, the *hourglass stabilization* must be adapted for material anisotropy. Therefore, a suitable approximation of the hourglass stiffness $\hat{\mathbb{C}}^{\mathrm{hg}}$ in Eq. (11) is needed. Schwarze and Reese [36,37] originally proposed a constant deviatoric matrix based on an effective shear modulus to prevent volumetric locking, according to the B-Bar method developed by Hughes [32]. However, this approximation has isotropic properties and underestimates the hourglass stresses for highly anisotropic materials, resulting in instabilities. An alternative hourglass stiffness based on the material tangent evaluated in the element center is proposed [65]

$$\hat{\mathbb{C}}^{\mathrm{hg}} = \left.\frac{\partial \hat{\boldsymbol{S}}(\hat{\boldsymbol{E}})}{\partial \hat{\boldsymbol{E}}}\right|_{\xi=\xi^0}, \tag{18}$$

which accounts for material anisotropy, while still allowing for an analytical integration in Eq. (16). This approach is limited to compressible materials as it does not conform with the B-bar method. However, the influence of potential volumetric locking is estimated to be negligible for the assumption of compressible engineering textiles in this work.

Second, a *membrane-bending decoupling* is a necessary requirement for textile forming. This can be accomplished intrinsically for individual elements with a specific out-of-plane integration scheme [13,69], variable stiffness over the thickness [16,17] or generalized continua approaches [21,22]. Based on these ideas and in combination with the Taylor approximation of the strains in Eq. (10), and a St. Venant-Kirchhoff material [23], the following split is introduced to the stress during the integration in Eq. (15)

$$\hat{\boldsymbol{S}}^{\star} = \hat{\boldsymbol{S}}^{\mathrm{M}} + \hat{\boldsymbol{S}}^{\mathrm{B}} = \hat{\mathbb{C}}^{\mathrm{M}} : (\hat{\boldsymbol{E}}_{\mathrm{c}}^{0} + \hat{\boldsymbol{E}}_{\mathrm{e}}) + \hat{\mathbb{C}}^{\mathrm{B}} : \left(\zeta \hat{\boldsymbol{E}}_{\mathrm{c}}^{\zeta} + \zeta^2 \hat{\boldsymbol{E}}_{\mathrm{c}}^{\zeta\zeta}\right). \tag{19}$$

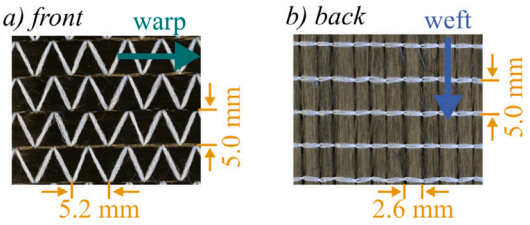

Fig. 2. Bidirectional non-crimp fabric MD600 from the (a) front and (b) back.

The material part $\hat{\boldsymbol{S}}^{\mathrm{M}}$, comprising the in-plane membrane and the out-of-plane compaction behavior, is related to the constant compatible strain in the element center $\hat{\boldsymbol{E}}_{\mathrm{c}}^{0}$ and the enhanced strains $\hat{\boldsymbol{E}}_{\mathrm{e}}$ by a material stiffness $\hat{\mathbb{C}}^{\mathrm{M}}$. The bending part $\hat{\boldsymbol{S}}^{\mathrm{B}}$ is related to the out-of-plane compatible strains $\hat{\boldsymbol{E}}_{\mathrm{c}}^{\zeta}$ and $\hat{\boldsymbol{E}}_{\mathrm{c}}^{\zeta\zeta}$ by a bending stiffness $\hat{\mathbb{C}}^{\mathrm{B}}$.

A major advantage of these modifications to the solid-shell formulation is that there are no restrictions on the three-dimensional stiffnesses $\hat{\mathbb{C}}^{(\star)}$ and that more complex formulations for $\hat{\boldsymbol{S}}^{\star}$ can be introduced based on the same split. The modified solid-shell is implemented as a Vuel user-defined element formulation in Abaqus/Explicit. A flowchart of the implementation concept is shown in Fig. A.9 with more details in [70].

3. Material model for textile forming

3.1. Investigated material

In this work, a nearly balanced bidirectional non-crimp fabric (NCF) without binder is applied to demonstrate the capabilities of the solid-shell formulation for textile forming. The fabric called MD600 is manufactured by Zoltek™ with an initial thickness of t_0 =1.004 mm and consists of two layers of carbon fibers, each weighing approximately 300 g m^{-2}. They are sewn together in a 0°/90° orientation in a tricot stitching pattern, cf. Fig. 2.

3.2. Material behavior - Membrane and compaction

The material stiffness tensor in Voigt notation is diagonal because Poission effects are neglected, as commonly assumed for textiles [1,2]

$$\hat{\mathbb{C}}^{\mathrm{M}} \triangleq \begin{bmatrix} C_{11}^{\mathrm{M}} & 0 & 0 & 0 & 0 & 0 \\ 0 & C_{22}^{\mathrm{M}} & 0 & 0 & 0 & 0 \\ 0 & 0 & C_{33}^{\mathrm{M}} & 0 & 0 & 0 \\ 0 & 0 & 0 & C_{12}^{\mathrm{M}} & 0 & 0 \\ 0 & 0 & 0 & 0 & C_{23}^{\mathrm{M}} & 0 \\ 0 & 0 & 0 & 0 & 0 & C_{13}^{\mathrm{M}} \end{bmatrix}. \tag{20}$$

The warp and weft stiffnesses are assumed as sufficiently high constant values ($C_{11}^{\mathrm{M}} = C_{22}^{\mathrm{M}} = 1000$ MPa) instead of a numerically complex inextensibility condition. This common assumption [13,19] effectively limits roving deformation during forming by preventing significant tensile strain. The transverse shear stiffnesses are assumed as sufficiently low constant values ($C_{23}^{\mathrm{M}} = C_{13}^{\mathrm{M}} = 0.1$ MPa) to prevent residual influences on the bending behavior. Parameter sensitivity studies have shown this holds true as long as the order of magnitude is equal to or smaller than the order of magnitude used for bending stiffness, cf. Section 3.3.

3.2.1. In-plane membrane behavior - Shear

The main deformation mode of the in-plane membrane behavior of the bidirectional NCF is assumed to be pure-shear. The validity of this assumption was demonstrated for the investigated bidirectional NCF in a previous study [71]. A fourth-order polynomial function is used to describe the shear stiffness of bidirectional fabrics [5,11,13]

$$C_{12}^{\mathrm{M}}\left(E_{\mathrm{c},12}^{0}\right) = \sum_{i=0}^{4} s_i \left(E_{\mathrm{c},12}^{0}\right)^{i}. \tag{21}$$

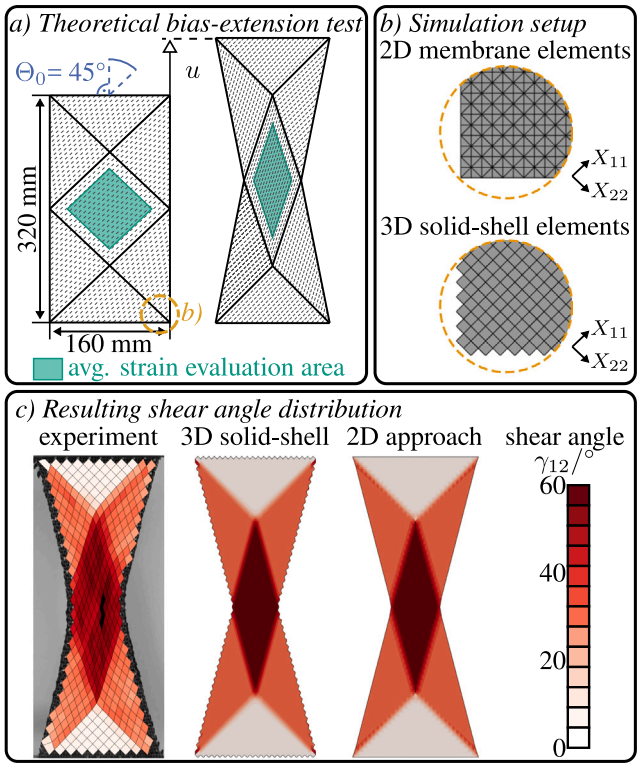

Fig. 3. (a) Theoretical deformation of the bias extension test (adapted from [72]); (b) Numerical mesh for the 2D and 3D approach; (c) Comparison of the experimentally measured and predicted shear angles at a displacement of 60 mm.

Bias extension tests (BET) with an initial length l_0 =320 mm, width w_0 =160 mm and fiber orientation Θ_0 =45° are conducted with a displacement u = 60 mm to parameterize the shear behavior, cf. Fig. 3a. The experimental results are detailed in [72].

The shear angle γ in the specimen was measured via digital image correlation (DIC), cf. Fig. 3c, and averaged in the center. The second Piola Kirchhoff shear stress S_{12} is incrementally calculated from the machine force f based on the energetic approach proposed by Boisse et al. [73]

$$S_{12}(\gamma) = f(\gamma)\frac{(l_0 - w_0)\left(\cos\left(\frac{\gamma}{2}\right) - \sin\left(\frac{\gamma}{2}\right)\right)}{w_0^2 t_0 \cos(\gamma)} - \frac{\cos\left(\frac{\gamma}{2}\right)}{2\cos(\gamma)} S_{12}\left(\frac{\gamma}{2}\right). \tag{22}$$

The resulting experimental shear stress is shown in Fig. 4a. The shear stiffness C_{12}^{M} is fitted to the experimental shear stress with a Nelder–Mead algorithm to determine a 'best-fit' parameter set, cf. Fig. 4a. For this purpose, the pure-shear assumption is applied with $E_{12} = {}^1/_2\cos({}^\pi/_2 - \gamma)$. The identified shear parameters for Eq. (21) are listed in Table B.1.

BET simulation and comparison to 2D approach. The solid-shell element is applied to simulations of the BET to verify the modeling approach. In addition, a conventional 2D element approach with an existing hyperelastic model for NCF [71,74] is used for comparison. The 2D approach is implemented by means of a user-defined material behavior (VUMAT) and applied to triangular membrane elements (M3D3). The same shear stiffness, cf. Eq. (21), with the same material parameters is used to define the pure shear-based energy potential. To ensure pure shear during the BET simulations, it is essential to avoid intra-ply tensile locking resulting from numerical tensile strains in the fiber directions of composite reinforcements. Thus, for both approaches, cf. Fig. 3b, the element edges are initially aligned in fiber direction, as recommended by Thije and Akkermann [75]. Alternatively, future work could modify the hourglass stabilization method to enable unaligned meshes and prevent potential locking in cases of high in-plane tension, as demonstrated by Hamila and Boisse [76,77].

The resulting shear angle distributions are shown in Fig. 3c. The averaged shear angle in the center and resulting forces are shown in Fig. 4b and c. For both modeling approaches, the predicted shear angle initially aligns with the pure-shear assumption for displacements u <30 mm. For larger displacements, the experimentally measured shear angle in the center is smaller due to relative roving slippage [72], leading to slight deviations in the predicted forces and shear strains. Overall, the results for the 3D solid-shell element and 2D approach are in good agreement with direct transferability of the material parameters. Both approaches provide a decent approximation of the membrane behavior of the investigated bidirectional NCF.

3.2.2. Out-of-plane compaction behavior

The main deformation mode of the out-of-plane material behavior is assumed to be compaction. An exponential function is used to describe the compaction stiffness

$$C_{33}^{\mathrm{M}}\left(E_{\mathrm{c},33}^0\right) = c_0 e^{c_1\left(E_{\mathrm{c},33}^0\right)^{c_2}}. \tag{23}$$

Plate-to-plate compaction tests on a single bidirectional NCF layer are conducted to parameterize the solid-shell. The experimental results are detailed in [70,78] and can be analytically described with a two-parameter power model for a pressure-dependent fiber volume content Φ as initially proposed by Robitaille and Gauvin [79]:

$$\Phi(p) = A \cdot p_{\mathrm{n}}^B \quad \text{with} \quad p_{\mathrm{n}} = \frac{p}{1\,\mathrm{kPa}}, \tag{24}$$

where A and B can be referred to as the initial fiber volume content at the unit compaction pressure and the growth parameter, respectively. The compaction pressure over layer thickness results are shown in Fig. 5. Good agreement between the experimental results and prediction of the solid-shell are achieved. The compaction parameters of the experiment and the simulation model are listed in Table B.2.

3.3. Bending behavior

The bending stiffness tensor in Voigt notation is again diagonal

$$\hat{\mathbb{C}}^{\mathrm{B}} \hat{=} \begin{bmatrix} C_{11}^{\mathrm{B}} & 0 & 0 & 0 & 0 & 0 \\ 0 & C_{22}^{\mathrm{B}} & 0 & 0 & 0 & 0 \\ 0 & 0 & C_{33}^{\mathrm{B}} & 0 & 0 & 0 \\ 0 & 0 & 0 & C_{12}^{\mathrm{B}} & 0 & 0 \\ 0 & 0 & 0 & 0 & C_{23}^{\mathrm{B}} & 0 \\ 0 & 0 & 0 & 0 & 0 & C_{13}^{\mathrm{B}} \end{bmatrix}. \tag{25}$$

The bending stiffness components of the bidirectional NCF is assumed to be constant, which is a common approximation for engineering textiles [3,11]. The bending compaction stiffness, related to changes in strain over the thickness, is assumed as sufficiently low ($C_{33}^{\mathrm{B}} = 0.1$ MPa) to model compaction completely via the material compaction behavior. The bending transverse shear stiffnesses are also assumed as sufficiently low ($C_{23}^{\mathrm{B}} = C_{13}^{\mathrm{B}} = 0.1$ MPa) due to their negligible influence for thin structures, as shown in parameter sensitivity studies [80]. The remaining bending stiffnesses in warp and weft direction (C_{11}^{B} and C_{22}^{B}) as well as shear (C_{12}^{B}) are determined experimentally with cantilever bending tests. The experimental results are detailed in [70]. The numerical bending stiffnesses are inversely identified by modeling the respective tests in combination with a gradient based Nelder–Mead algorithm. The overhang length $l_{\mathrm{bend}}^{\mathrm{exp}}$ of the fabric in the individual configurations is chosen as the optimization goal, cf. Fig. 6. First, C_{11}^{B} and C_{22}^{B} are determined to match the cantilever tests with initial fiber orientations of $\Theta_0 = 0°$ and 90°, respectively. Second, C_{12}^{B} is determined to match the $\Theta_0 = 45°$ cantilever test. The identified bending parameters are listed in Table B.3.

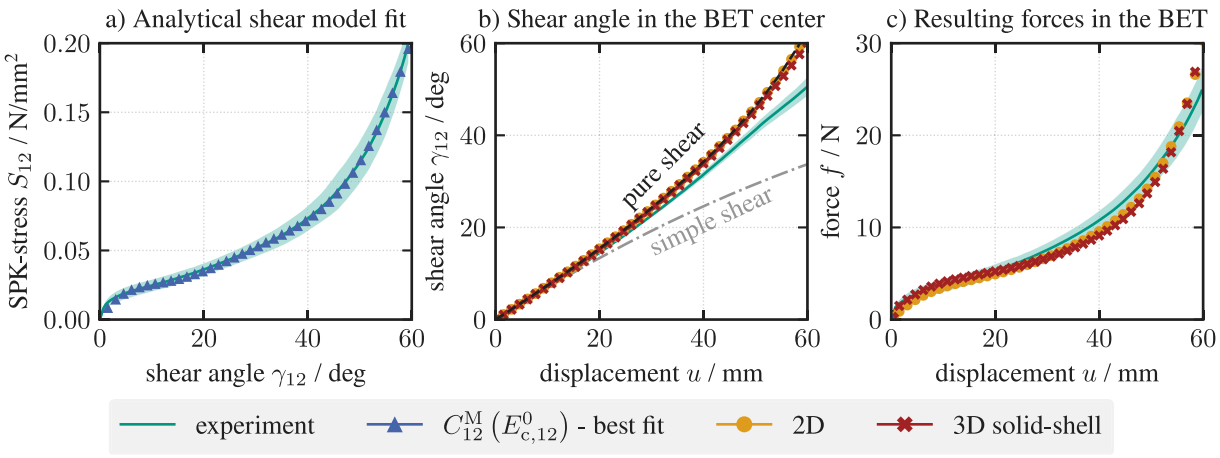

Fig. 4. (a) Parameterization of the shear stiffness based on the energetic approach by Boisse et al. [73]; (b) Overview of the shear angle in the center of the BET; (c) Resulting forces in the BET.

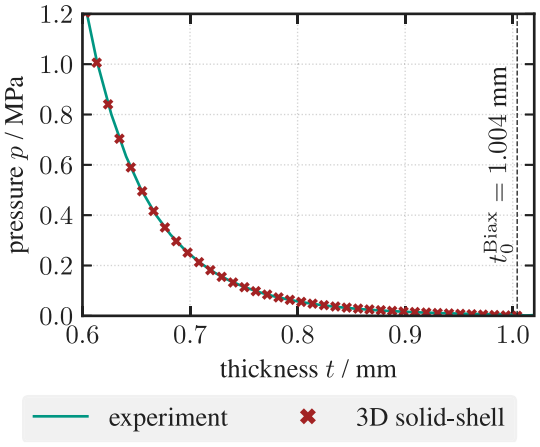

Fig. 5. Experimental and predicted compaction behavior.

Cantilever test simulation and comparison to 2D approach. In addition to the experimental tests and the solid-shell approach, a conventional 2D element approach with an existing hypoelastic model [19,71,74] is used for comparison. The 2D approach is implemented by means of a VUGENS subroutine for a user-defined shell section integration scheme over the thickness t_0 and applied to triangular shell elements (S3R). The same bending stiffnesses with the same material parameters as for the solid-shell can also be used for the 2D approach.

The resulting deflection curves during the cantilever tests are shown in Fig. 6. For both modeling approaches, the predictions for $\Theta_0 = 0°$ and 90° nearly align, but slightly deviate from the experimental results. This is because the assumed constant bending stiffness neglects the decrease for large curvatures typically measured in textiles [17,70,81]. Differences in the 45°-cantilever tests are due to the different element shapes of the 2D and 3D approaches, with the solid-shell slightly better agreeing with the experimental results. Overall, the results for the 3D solid-shell element and 2D approach are in good agreement with direct transferability of the material parameters. Both approaches provide a decent approximation of the bending behavior of the investigated bidirectional NCF.

4. Validation of forming behavior

4.1. Setup of forming tests

The proposed 3D solid-shell element is applied to forming simulations of a hemisphere geometry for validation. It is compared to a conventional 2D approach based on superimposed triangular membrane and shell elements, cf. Section 3.2.1 and Section 3.3, respectively. A comparison with commercial 3D solid elements was not pursued because these elements cannot model the forming behavior of thin textiles due to numerical locking and a lack of a membrane-bending decoupling [64,65]. Similarly, the continuum shell elements available in Abaqus/Explicit were not used because they require a superimposed user element to model nonlinear compaction and cannot model anisotropic decoupled bending behavior, as demonstrated by Poppe et al. [5].

A single (0°/90°)-layer is formed with a depth of $u^{\mathrm{punch}} = 75$ mm and blank dimensions of 300 mm x 300 mm. The general contact algorithm in ABAQUS/EXPLICIT is applied to model friction between the tools and the fabric. A friction coefficient of $\mu = 0.157$ was determined in sled pull-over tests, which are detailed in [82]. For both modeling approaches, initial element edge lengths of $l_0 = 5$ mm and a thickness of $t_0 = 1.004$ mm are applied, with the element edges initially aligned in fiber direction to avoid intra-ply tensile locking [75,76], cf. Section 3.2.1. The textile layer is modeled using 7200 superimposed membrane M3D3 and shell S3R triangular elements with a computation time of approx. 10 min, or 3600 solid-shell elements with a computation time of approx. 60 min, both on six cores of an AMD EPYC 7313P processor.

Two configurations are considered to validate the new solid-shell approach, both based on a hemisphere punch and a matching hole plate as lower tool. First, a setup with planar blank holder of 1.7 kg is applied to prevent out-of-plane deformation outside the hemisphere's center and focus on the membrane behavior, cf. Fig. 7a. For this configuration, experimental results are available in [83]. Transparent tools and a pattern of white dots on the textile are applied to enable a measurement of the shear angle in the closed configuration via a 2D-DIC [72,83]. Second, the same setup without the blank holder is applied to focus on the bending behavior, cf. Fig. 8a.

4.2. Hemisphere forming with blank holder

The experimental and the predicted outer contour of the blank after forming with a planar blank holder is shown in Fig. 7c. The outer contour can be used to evaluate the overall deformation behavior based

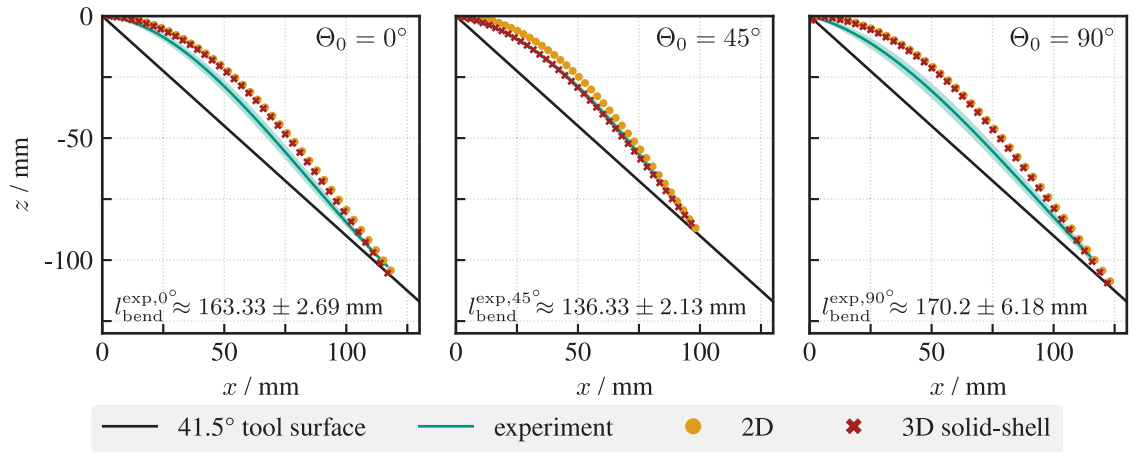

Fig. 6. Experimental and predicted deflections curves during the cantilever tests with initial orientations of Θ_0 = 0°, 45° and 90°.

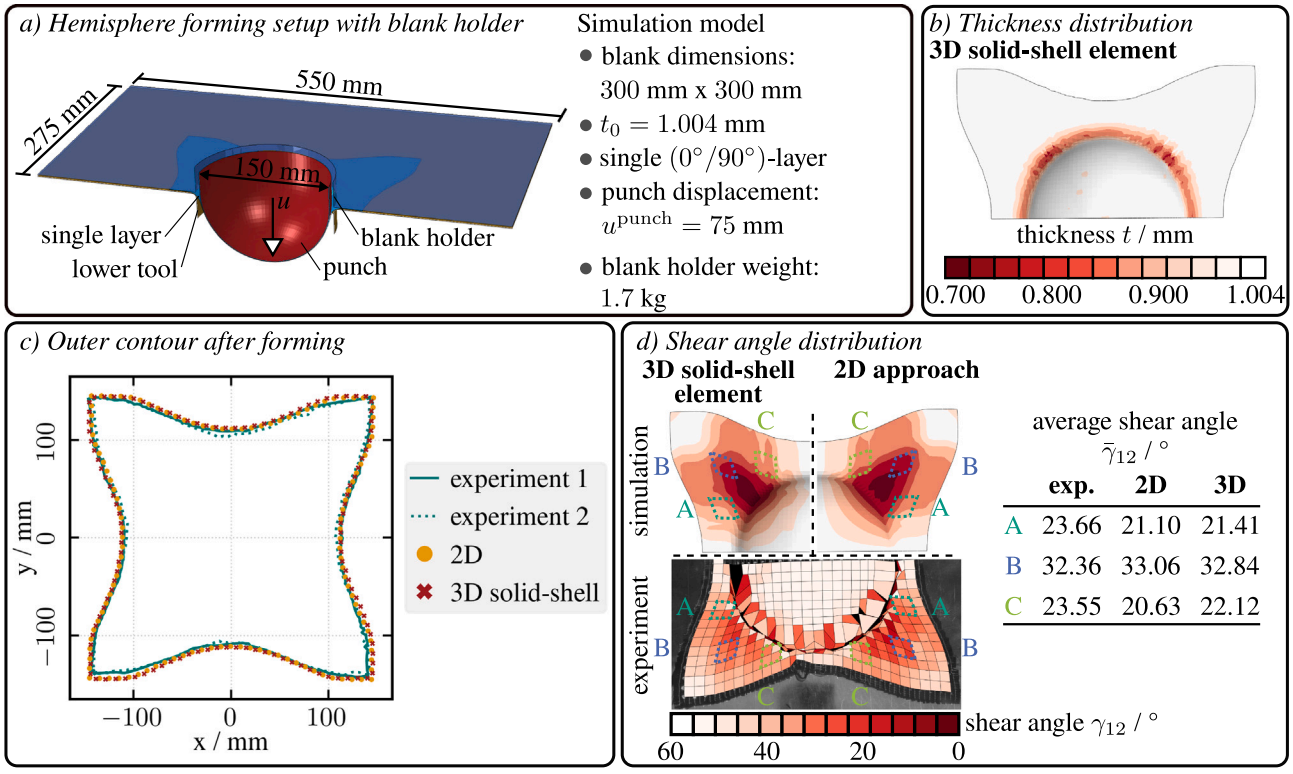

Fig. 7. Hemisphere forming tests with blank holder for experimental validation | (a) Setup of the simulation model, showing only a view cut of the model due to symmetry; (b) Thickness distribution after forming; (c) Outer contour after forming; (d) Shear angle distribution after forming.

on the material draw-in [15,74]. The 2D approach with superimposed elements and the 3D solid-shell are in good quantitative agreement with each other and the experiments. A strong material draw-in in the principal fiber directions is observed. The material mainly deforms under shear with negligible strains in both fiber directions. This indicates an adequate modeling of the bidirectional NCF's general deformation behavior by the pure-shear assumption.

The experimental and predicted shear angle distribution after forming is shown in Fig. 7d. The general location and shape of areas with high shear angles are predicted well by the 2D and 3D approach. For a more detailed comparison, the average shear angles $\bar{\gamma}_{12}$ in three distinct local areas (A, B, C) are calculated. The 2D approach with superimposed elements and the 3D solid-shell are in good quantitative agreement with the experiments at $\Delta\bar{\gamma}_{12} < 3°$.

The final thickness of the blank can be evaluated for the solid-shell element and is shown in Fig. 7b. A direct comparison with experimental results is not possible due to the lack of an in-situ thickness measurement capability and the absence of a binder for subsequent measurement. The low weight of the blank holder does not lead to a significant change in thickness in the flat areas. This is consistent with the experimental thickness measurements during the plate-to-plate compaction trials [70,78]. In the hemisphere center, the thickness also does not change significantly, as no closed lower tool is used. The

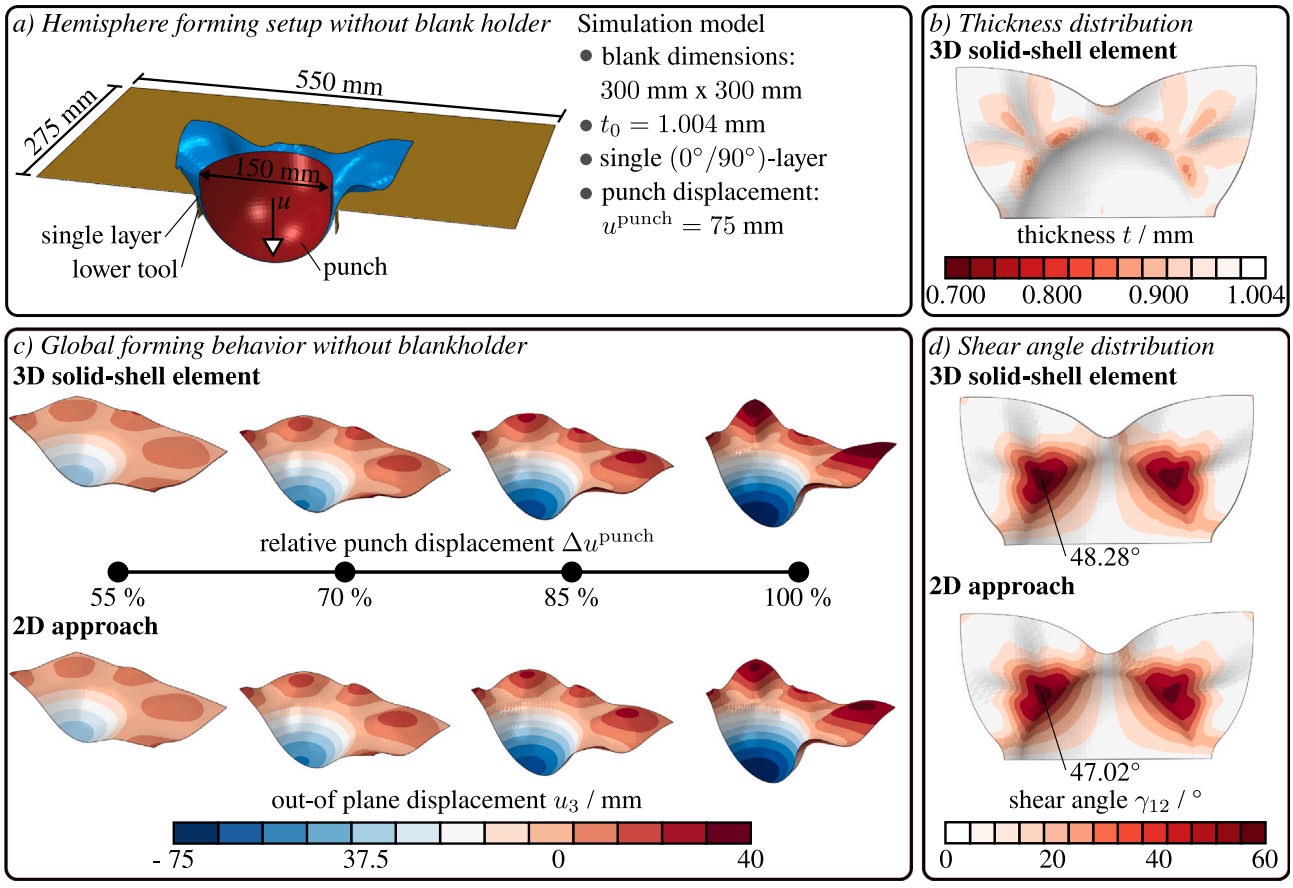

Fig. 8. Hemisphere forming tests without blank holder for numerical verification | (a) Setup of the simulation model, showing only a view cut of the model due to symmetry; (b) Thickness distribution after forming; (c) Global forming behavior represented by the out-of-plane displacements; (d) Shear angle distribution after forming (maximum values shown).

greatest change in thickness occurs in the area of the radius, where noticeable thinning occurs, which qualitatively matches the experimental results for a comparable bidirectional textile [84].

4.3. Hemisphere forming without blank holder

The global forming behavior of the 2D approach and 3D solid-shell element during the hemisphere forming without a blank holder for different relative punch displacements Δu^{punch} is shown in Fig. 8c. Good agreement between the two approaches is achieved for the predicted locations of out-of-plane displacements with only minor deviations in magnitude. This indicates a locking-free bending behavior and correct description of the membrane-bending decoupling by the solid-shell element. The predicted global forming behavior also qualitatively matches with experimental results for a woven fabric [15,85] or bidirectional NCF [17]. The predicted shear angle distribution of the 2D approach and 3D solid-element are also in good agreement, cf. Fig. 8d.

The final thickness distribution for the solid-shell element is shown in Fig. 8b. Compared to the setup with planar blank holder, cf. Fig. 7b, thinning no longer occurs along the entire radius. Instead, slight thinning is concentrated in areas of out-of-plane deformation due to the transverse pressure during wrinkle formation.

5. Conclusion and outlook

The consideration of compaction during forming is necessary to predict the final thickness distribution in a formed component and consequently the local permeability, necessary press forces as well as mechanical properties. This requires a three-dimensional material behavior in an appropriate element formulation. A new 8-node hexahedral solid-shell element for macroscopic forming simulation of engineering textiles is proposed. The formulation is based solely on displacement DOFs and combines a selective reduced integration scheme (SRI), the assumed natural strain method (ANS) with four collocation points and the enhanced assumed strain method (EAS) with one EAS-DOF to avoid numerical locking. For application to textile forming, a new hourglass stabilization method for highly anisotropic materials and a membrane-bending decoupling based on a Taylor expansion of the strain in thickness direction are introduced. The solid-shell is implemented as a user-defined element VUEL in the FE solver ABAQUS/EXPLICIT.

The proposed solid-shell is parameterized for a bidirectional non-crimp fabric based on bias extension, plate-to-plate compaction and cantilever bending tests. Good agreement with the experimental results is achieved. The in-plane shear and out-of plane bending behavior is also comparable to the predictions of a conventional 2D approach with superimposed membrane and shell elements for an extrinsic membrane-bending decoupling. Finally, the solid-shell is applied to hemisphere forming tests for validation. In the setup with a planar blank holder focussing on the membrane behavior, good agreement with experimental results and predictions of the 2D approach are achieved for the outer contour and shear angle distribution after forming. In the setup without blank holder focussing on the bending behavior, good agreement with the 2D approach is achieved for the global forming behavior and shear angle distribution. Both tests demonstrate the locking-free behavior and correct description of the membrane-bending decoupling by the solid-shell element. In addition, the final thickness of the textile after forming can be evaluated with qualitatively plausible predictions in comparison to literature. However, quantitative validation of the thickness should be a focus of future studies.

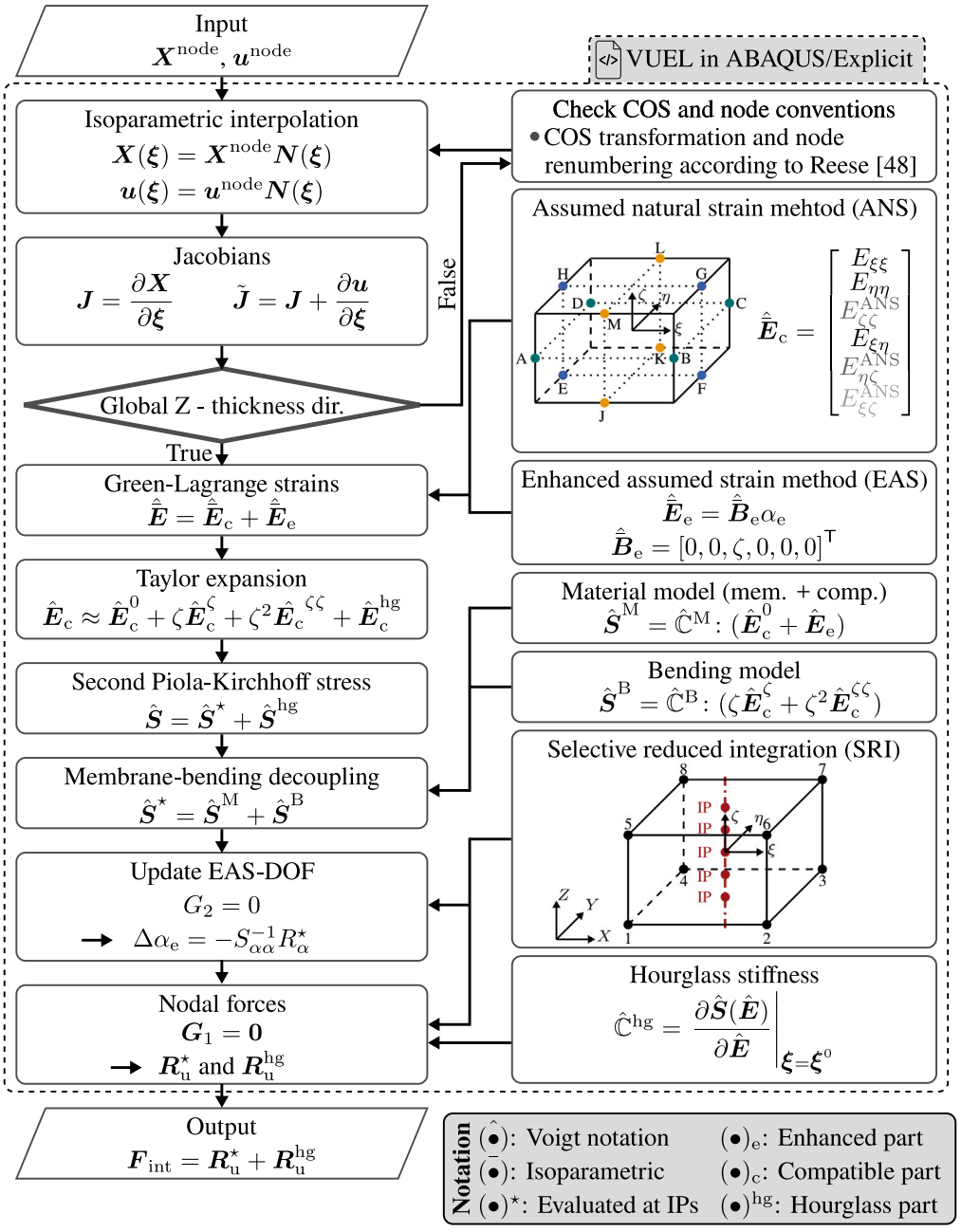

Fig. A.9. Flowchart of the solid-shell implemented as a VUEL in ABAQUS/EXPLICIT.
Source: (adapted from [70]).

In conclusion, a new 3D solid-shell formulation for forming simulation of engineering textiles is presented and validated with three main advantages. First, it can model the forming behavior with an intrinsic membrane-bending decoupling within a single element based on displacement DOF. This enables an implementation in FE solvers without specific requirements on external DOF. Second, it requires only a single element over the thickness. This enables direct transferability of material parameters and methods developed for 2D approaches. Third, it can model forming processes as accurately as 2D approaches, but with the additional prediction of the behavior in thickness direction.

The solid-shell element is developed without restrictions on the applied material model and could be utilized in future investigations for other engineering textiles or pre-infiltrated semi-finished products. The utilization of a fully three-dimensional approach should enable a better approximation of forming effects like the fiber volume content and improve the prediction quality of subsequent process steps when embedded in a CAE chain [86]. Especially for LCM processes such as wet compression molding with strong fluid–structure interaction, this formulation could be used for simultaneous modeling of forming and infiltration. By combining it with the fluid propagation sub-model of Poppe et al. [5], their models' previous limitation of a lack of a membrane-bending decoupling when using conventional 3D elements could be overcome. In addition, the three-dimensional constitutive law could be exploited to introduce relevant couplings for multi-axial stress states, which cannot be modeled with 2D approaches. This would enable the modeling of effects like a shear-compaction coupling, which is observed in woven fabrics [87], or shear-induced thickening, which is observed in NCFs and woven fabrics [88].

Table B.1
Material parameters of the shear behavior.

s_0 MPa	s_1 MPa	s_2 MPa	s_3 MPa	s_4 MPa
0.1919	−2.3637	14.7593	−40.7199	42.3208

Table B.2
Material parameters of the compaction behavior.

	A –	B –	
experiment	0.2820	0.0926	
	c_0 MPa	c_1 –	c_2 –
simulation	0.1563	60.4653	2.4528

Table B.3
Material parameters of the bending behavior.

C^B_{11} MPa	C^B_{22} MPa	C^B_{33} MPa	C^B_{12} MPa	C^B_{23} MPa	C^B_{13} MPa
38.0615	43.0668	0.1000	4.2123	0.1000	0.1000

CRediT authorship contribution statement

Bastian Schäfer: Writing – original draft, Validation, Software, Methodology, Investigation, Conceptualization. **Johannes Mitsch:** Writing – review & editing, Software, Methodology, Conceptualization. **Luise Kärger:** Writing – review & editing, Supervision, Project administration, Funding acquisition, Conceptualization.

Declaration of competing interest

The authors declare that they have no known competing financial interests or personal relationships that could have appeared to influence the work reported in this paper.

Acknowledgments

The authors would like to thank the Deutsche Forschungsgemeinschaft (DFG, German Research Foundation) for funding the AI Research Unit 5339 (project no. 459291153). This work is also part of the Heisenberg project “Digitalization of fiber-reinforced polymer processes for resource-efficient manufacturing of lightweight components” funded by the Deutsche Forschungsgemeinschaft (DFG, German Research Foundation) (project no. 455807141). The authors thank the team of the LaMCoS laboratory at INSA Lyon, especially Ruochen Zheng, for conducting the hemisphere forming tests.

Appendix A. Implementation of the solid-shell

See Fig. A.9.

Appendix B. Material parameters

See Tables B.1–B.3.

Data availability

Data will be made available on request.

References

[1] Liang B, Boisse P. A review of numerical analyses and experimental characterization methods for forming of textile reinforcements. Chin J Aeronaut 2021;34(8):143–63. http://dx.doi.org/10.1016/j.cja.2020.09.027.
[2] Bussetta P, Correia N. Numerical forming of continuous fibre reinforced composite material: A review. Compos Part A: Appl Sci Manuf 2018;113:12–31. http://dx.doi.org/10.1016/j.compositesa.2018.07.010.
[3] Boisse P, Colmars J, Hamila N, Naouar N, Steer Q. Bending and wrinkling of composite fiber preforms and prepregs. A review and new developments in the draping simulations. Compos Part B: Eng 2018;141:234–49. http://dx.doi.org/10.1016/j.compositesb.2017.12.061.
[4] Xie J, Guo Z, Shao M, Zhu W, Jiao W, Yang Z, et al. Mechanics of textiles used as composite preforms: A review. Compos Struct 2023;304:116401. http://dx.doi.org/10.1016/j.compstruct.2022.116401.
[5] Poppe CT, Krauß C, Albrecht F, Kärger L. A 3D process simulation model for wet compression moulding. Compos Part A: Appl Sci Manuf 2021;50(17):106379. http://dx.doi.org/10.1016/j.compositesa.2021.106379.
[6] Lomov SV, Verpoest I, Peeters T, Roose D, Zako M. Nesting in textile laminates: geometrical modelling of the laminate. Compos Sci Technol 2003;63(7):993–1007. http://dx.doi.org/10.1016/S0266-3538(02)00318-4.
[7] Potluri P, Sagar TV. Compaction modelling of textile preforms for composite structures. Compos Struct 2008;86(1–3):177–85. http://dx.doi.org/10.1016/j.compstruct.2008.03.019.
[8] Nguyen QT, Vidal-Sallé E, Boisse P, Park CH, Saouab A, Bréard J, et al. Mesoscopic scale analyses of textile composite reinforcement compaction. Compos Part B: Eng 2013;44(1):231–41. http://dx.doi.org/10.1016/j.compositesb.2012.05.028.
[9] Colin D, Bel S, Hans T, Hartmann M, Drechsler K. Virtual description of non-crimp fabrics at the scale of filaments including orientation variability in the fibrous layers. Appl Compos Mater 2020;27(4):337–55. http://dx.doi.org/10.1007/s10443-020-09819-1.
[10] Bublitz D. A material model for the compaction process simulation of carbon fiber preforms (Dissertation), Munich, Germany: Technical University of Munich; 2023.
[11] Boisse P, Hamila N, Vidal-Sallé E, Dumont F. Simulation of wrinkling during textile composite reinforcement forming. Influence of tensile, in-plane shear and bending stiffnesses. Compos Sci Technol 2011;71(5):683–92. http://dx.doi.org/10.1016/j.compscitech.2011.01.011.
[12] Boisse P, Borr M, Buet K, Cherouat A. Finite element simulations of textile composite forming including the biaxial fabric behaviour. Compos Part B: Eng 1997;28(4):453–64. http://dx.doi.org/10.1016/S1359-8368(96)00067-4.
[13] Allaoui S, Boisse P, Chatel S, Hamila N, Hivet G, Soulat D, et al. Experimental and numerical analyses of textile reinforcement forming of a tetrahedral shape. Compos Part A: Appl Sci Manuf 2011;42(6):612–22. http://dx.doi.org/10.1016/j.compositesa.2011.02.001.
[14] Dörr D, Henning F, Kärger L. Nonlinear hyperviscoelastic modelling of intra-ply deformation behaviour in finite element forming simulation of continuously fibre-reinforced thermoplastics. Compos Part A: Appl Sci Manuf 2018;109:585–96. http://dx.doi.org/10.1016/j.compositesa.2018.03.037.
[15] Chen B, Colmars J, Naouar N, Boisse P. A hypoelastic stress resultant shell approach for simulations of textile composite reinforcement forming. Compos Part A: Appl Sci Manuf 2021;149(4):106558. http://dx.doi.org/10.1016/j.compositesa.2021.106558.
[16] Döbrich O, Gereke T, Diestel O, Krzywinski S, Cherif C. Decoupling the bending behavior and the membrane properties of finite shell elements for a correct description of the mechanical behavior of textiles with a laminate formulation. J Ind Text 2014;44(1):70–84. http://dx.doi.org/10.1177/1528083713477442.
[17] Yu F, Chen S, Harper LT, Warrior NA. Simulating the effect of fabric bending stiffness on the wrinkling behaviour of biaxial fabrics during preforming. Compos Part A: Appl Sci Manuf 2021;143(2071):106308. http://dx.doi.org/10.1016/j.compositesa.2021.106308.
[18] Haanappel SP, ten Thije R, Sachs U, Rietman B, Akkerman R. Formability analyses of uni-directional and textile reinforced thermoplastics. Compos Part A: Appl Sci Manuf 2014;56:80–92. http://dx.doi.org/10.1016/j.compositesa.2013.09.009.
[19] Dörr D, Schirmaier FJ, Henning F, Kärger L. A viscoelastic approach for modeling bending behavior in finite element forming simulation of continuously fiber reinforced composites. Compos Part A: Appl Sci Manuf 2017;94:113–23. http://dx.doi.org/10.1016/j.compositesa.2016.11.027.
[20] Poppe C, Rosenkranz T, Dörr D, Kärger L. Comparative experimental and numerical analysis of bending behaviour of dry and low viscous infiltrated woven fabrics. Compos Part A: Appl Sci Manuf 2019;124:105466. http://dx.doi.org/10.1016/j.compositesa.2019.05.034.
[21] Barbagallo G, Madeo A, Morestin F, Boisse P. Modelling the deep drawing of a 3D woven fabric with a second gradient model. Math Mech Solids 2017;22(11):2165–79. http://dx.doi.org/10.1177/1081286516663999.
[22] Boisse P, Bai R, Colmars J, Hamila N, Liang B, Madeo A. The need to use generalized continuum mechanics to model 3D textile composite forming. Appl Compos Mater 2018;47(11). http://dx.doi.org/10.1007/s10443-018-9719-8.

[23] Belytschko T, Liu WK, Moran B, Elkhodary KI. Nonlinear finite elements for continua and structures. 2nd ed.. Chichester, UK: John Wiley & Sons, Ltd; 2014.

[24] Mathieu S, Hamila N, Bouillon F, Boisse P. Enhanced modeling of 3D composite preform deformations taking into account local fiber bending stiffness. Compos Sci Technol 2015;117:322–33. http://dx.doi.org/10.1016/j.compscitech.2015.07.005.

[25] Mathieu S, Hamila N, Dupé F, Descamps C, Boisse P. Stability of 3D textile composite reinforcement simulations: Solutions to spurious transverse modes. Appl Compos Mater 2016;23(4):739–60. http://dx.doi.org/10.1007/s10443-016-9483-6.

[26] Ferretti M, Madeo A, dell'Isola F, Boisse P. Modeling the onset of shear boundary layers in fibrous composite reinforcements by second-gradient theory. Z Angew Math Phys 2014;65(3):587–612. http://dx.doi.org/10.1007/s00033-013-0347-8.

[27] Madeo A, Ferretti M, dell'Isola F, Boisse P. Thick fibrous composite reinforcements behave as special second-gradient materials: three-point bending of 3D interlocks. Z Für Angew Math Und Phys 2015;66(4):2041–60. http://dx.doi.org/10.1007/s00033-015-0496-z.

[28] Barbagallo G, D'Agostino MV, Aivaliotis A, Daouadji A, Makradi A, Giunta G, et al. Model reduction for the forming process of fibrous composites structures via second gradient enriched continuum models. Mech Adv Mater Struct 2021;28(10):1061–72. http://dx.doi.org/10.1080/15376494.2019.1629050.

[29] Bischoff M. Theorie und Numerik einer dreidimensionalen Schalenformulierung (Dissertation), Stuttgart, Germany: Institut für Baustatik und Baudynamik, University of Stuttgart; 1999, http://dx.doi.org/10.18419/opus-126, [in German].

[30] Koschnick F. Geometrische Locking-Effekte bei Finiten Elementen und ein allgemeines Konzept zu ihrer Vermeidung (Dissertation), Munich, Germany: Fakultät für Bauingenieur– und Vermessungswesen, Technical University of Munich; 2004, [in German].

[31] Wagner M. Lineare und nichtlineare FEM: Eine Einführung mit Anwendungen in der Umformsimulation mit LS-DYNA, 2nf ed.. Wiesbaden, Germany: Springer Vieweg; 2019, http://dx.doi.org/10.1007/978-3-658-25052-2.

[32] Hughes TJR. Generalization of selective integration procedures to anisotropic and nonlinear media. Int J Numer Methods Eng 1980;15(9):1413–8. http://dx.doi.org/10.1002/nme.1620150914.

[33] Bathe K-J, Dvorkin EN. A formulation of general shell elements-the use of mixed interpolation of tensorial components. Int J Numer Methods Eng 1986;22:697–722. http://dx.doi.org/10.1002/nme.1620220312.

[34] Simo JC, Rifai MS. A class of mixed assumed strain methods and the method of incompatible modes. Int J Numer Methods Eng 1990;29(8):1595–638. http://dx.doi.org/10.1002/nme.1620290802.

[35] Rah K, van Paepegem W, Habraken AM, de Sousa RA, Valente RAF. Evaluation of different advanced finite element concepts for detailed stress analysis of laminated composite structures. Int J Mater Form 2009;2(S1):943–7. http://dx.doi.org/10.1007/s12289-009-0629-z.

[36] Schwarze M, Reese S. A reduced integration solid-shell finite element based on the EAS and the ANS concept-geometrically linear problems. Int J Numer Methods Eng 2009;80(10):1322–55. http://dx.doi.org/10.1002/nme.2653.

[37] Schwarze M, Reese S. A reduced integration solid-shell finite element based on the EAS and the ANS concept-large deformation problems. Int J Numer Methods Eng 2011;85(3):289–329. http://dx.doi.org/10.1002/nme.2966.

[38] Mostafa M. An improved solid-shell element based on ANS and EAS concepts. Int J Numer Methods Eng 2016;108(11):1362–80. http://dx.doi.org/10.1002/nme.5260.

[39] Hauptmann R, Schweizerhof K. A systematic development of 'solid–shell' element formulations for linear and non–linear analyses employing only displacement degrees of freedom. Int J Numer Methods Eng 1998;42(1):49–69. http://dx.doi.org/10.1002/(SICI)1097-0207(19980515)42:1<49::AID-NME349>3.3.CO;2-U.

[40] Hauptmann R, Schweizerhof K, Doll S. Extension of the 'solid-shell' concept for application to large elastic and large elastoplastic deformations. Int J Numer Methods Eng 2000;49(9):1121–41. http://dx.doi.org/10.1002/1097-0207(20001130)49:9<1121::AID-NME130>3.0.CO;2-F.

[41] Hauptmann R, Doll S, Harnau M, Schweizerhof K. 'Solid-shell' elements with linear and quadratic shape functions at large deformations with nearly incompressible materials. Comput Struct 2001;79(18):1671–85. http://dx.doi.org/10.1016/S0045-7949(01)00103-1.

[42] Mattern S. Hocheffiziente Formulierung und Implementierung finiter Elemente für transiente Analysen mit expliziter Zeitintegration (Dissertation), Karlsruhe, Germany: Karlsruhe Institute of Technology; 2012, [in German].

[43] Mattern S, Schmied C, Schweizerhof K. Highly efficient solid and solid-shell finite elements with mixed strain–displacement assumptions specifically set up for explicit dynamic simulations using symbolic programming. Comput Struct 2015;154:210–25. http://dx.doi.org/10.1016/j.compstruc.2015.03.009.

[44] Vu-Quoc L, Tan XG. Optimal solid shells for non-linear analyses of multilayer composites. I. Statics. Comput Methods Appl Mech Eng 2003;192(9–10):975–1016. http://dx.doi.org/10.1016/S0045-7825(02)00435-8.

[45] Vu-Quoc L, Tan XG. Optimal solid shells for non-linear analyses of multilayer composites. II. Dynamics. Comput Methods Appl Mech Eng 2003;192(9–10):1017–59. http://dx.doi.org/10.1016/S0045-7825(02)00336-5.

[46] Vu-Quoc L, Tan X. Efficient Hybrid-EAS solid element for accurate stress prediction in thick laminated beams, plates, and shells. Comput Methods Appl Mech Eng 2013;253:337–55. http://dx.doi.org/10.1016/j.cma.2012.07.025.

[47] Reese S, Wriggers P, Reddy BD. A new locking-free brick element technique for large deformation problems in elasticity. Comput Struct 2000;75(3):291–304. http://dx.doi.org/10.1016/S0045-7949(99)00137-6.

[48] Reese S. A large deformation solid-shell concept based on reduced integration with hourglass stabilization. Int J Numer Methods Eng 2007;69(8):1671–716. http://dx.doi.org/10.1002/nme.1827.

[49] Alves de Sousa RJ, Cardoso RP, Fontes Valente RA, Yoon J-W, Grácio JJ, Natal Jorge RM. A new one-point quadrature enhanced assumed strain (EAS) solid-shell element with multiple integration points along thickness: Part I-geometrically linear applications. Int J Numer Methods Eng 2005;62(7):952–77. http://dx.doi.org/10.1002/nme.1226.

[50] Alves de Sousa RJ, Cardoso RPR, Fontes Valente RA, Yoon J-W, Grácio JJ, Natal Jorge RM. A new one-point quadrature enhanced assumed strain (EAS) solid-shell element with multiple integration points along thickness—part II: nonlinear applications. Int J Numer Methods Eng 2006;67(2):160–88. http://dx.doi.org/10.1002/nme.1609.

[51] Alves De Sousa R, Yoon J, Cardoso R, Fontes Valente R, Gracio J. On the use of a reduced enhanced solid-shell (RESS) element for sheet forming simulations. Int J Plast 2007;23(3):490–515. http://dx.doi.org/10.1016/j.ijplas.2006.06.004.

[52] Cardoso RPR, Yoon JW, Mahardika M, Choudhry S, Alves de Sousa RJ, Fontes Valente RA. Enhanced assumed strain (EAS) and assumed natural strain (ANS) methods for one–point quadrature solid–shell elements. Int J Numer Methods Eng 2008;75(2):156–87. http://dx.doi.org/10.1002/nme.2250.

[53] Pagani M, Reese S, Perego U. Computationally efficient explicit nonlinear analyses using reduced integration-based solid-shell finite elements. Comput Methods Appl Mech Eng 2014;268:141–59. http://dx.doi.org/10.1016/j.cma.2013.09.005.

[54] Simon J-W, Stier B, Reese S. A solid-shell finite element for fibre reinforced composites. Proc Appl Math Mech (PAMM) 2012;12(1):329–30. http://dx.doi.org/10.1002/pamm.201210153.

[55] Barfusz O, Smeenk R, Reese S. Solid-shell formulations based on reduced integration - investigations of anisotropic material behaviour at large deformations. Proc Appl Math Mech (PAMM) 2018;18(1):e201800078. http://dx.doi.org/10.1002/pamm.201800078.

[56] Schwarze M, Vladimirov IN, Reese S. Sheet metal forming and springback simulation by means of a new reduced integration solid-shell finite element technology. Comput Methods Appl Mech Eng 2011;200(5–8):454–76. http://dx.doi.org/10.1016/j.cma.2010.07.020.

[57] Robertsson K, Borgqvist E, Wallin M, Ristinmaa M, Tryding J, Giampieri A, et al. Efficient and accurate simulation of the packaging forming process. Packag Technol Sci 2018;31(8):557–66. http://dx.doi.org/10.1002/pts.2383.

[58] Dia M, Hamila N, Abbas M, Gravouil A. A nine nodes solid-shell finite element with enhanced pinching stress. Comput Mech 2020;65(5):1377–95. http://dx.doi.org/10.1007/s00466-020-01825-1.

[59] Chen QQ, Saouab A, Boisse P, Park CH, Bréard J. Woven thermoplastic composite forming simulation with solid-shell element method. Int J Simul Multidiscip Des Optim 2009;3(2):337–41. http://dx.doi.org/10.1051/ijsmdo/2009008.

[60] Chen Q, Boisse P, Park CH, Saouab A, Bréard J. Intra/inter-ply shear behaviors of continuous fiber reinforced thermoplastic composites in thermoforming processes. Compos Struct 2011;93(7):1692–703. http://dx.doi.org/10.1016/j.compstruct.2011.01.002.

[61] Xiong H, Guzman Maldonado E, Hamila N, Boisse P. A prismatic solid-shell finite element based on a DKT approach with efficient calculation of through the thickness deformation. Finite Elements Anal Des 2018;151:18–33. http://dx.doi.org/10.1016/j.finel.2018.08.003.

[62] Xiong H, Hamila N, Boisse P. Consolidation modeling during thermoforming of thermoplastic composite prepregs. Mater 2019;12(18):2853. http://dx.doi.org/10.3390/ma12182853.

[63] Poppe C, Albrecht F, Krauß C, Kärger L. A 3D modelling approach for fluid progression during process simulation of wet compression moulding – Motivation & approach. Procedia Manuf 2020;47:85–92. http://dx.doi.org/10.1016/j.promfg.2020.04.141.

[64] Schäfer B, Dörr D, Kärger L. Reduced-integrated 8-node hexahedral solid-shell element for the macroscopic forming simulation of continuous fibre-reinforced polymers. Procedia Manuf 2020;47:134–9. http://dx.doi.org/10.1016/j.promfg.2020.04.154.

[65] Schäfer B, Dörr D, Kärger L. Potential and challenges of a solid-shell element for the macroscopic forming simulation of engineering textiles. In: Proceedings of the 24th international conference on material forming. 2021, http://dx.doi.org/10.25518/esaform21.883.

[66] Betsch P, Stein E. An assumed strain approach avoiding artificial thickness straining for a non-linear 4-node shell element. Commun Numer Methods Eng 1995;11(11):899–909. http://dx.doi.org/10.1002/cnm.1640111104.

[67] Simo J, Armero F, Taylor R. Improved versions of assumed enhanced strain tri-linear elements for 3D finite deformation problems. Comput Methods Appl Mech Eng 1993;110:359–86. http://dx.doi.org/10.1016/0045-7825(93)90215-J.

[68] Macneal RH, Harder RL. A proposed standard set of problems to test finite element accuracy. Finite Elem Anal Des 1985;1(1):3–20. http://dx.doi.org/10.1016/0168-874X(85)90003-4.

[69] Dörr D, Joppich T, Kugele D, Henning F, Kärger L. A coupled thermo-mechanical approach for finite element forming simulation of continuously fiber-reinforced semi-crystalline thermoplastics. Compos Part A: Appl Sci Manuf 2019;125:105508. http://dx.doi.org/10.1016/j.compositesa.2019.105508.

[70] Schäfer B. Macroscopic forming simulation of unidirectional non-crimp fabrics: Hyperelastic material modeling and 3D-solid-shell approach (Dissertation), Karlsruhe, Germany: Karlsruhe Institute of Technology (KIT); 2024, http://dx.doi.org/10.5445/IR/1000170739.

[71] Schäfer B, Dörr D, Naouar N, Wank JP. Capabilities and limitations of pure-shear based macroscopic forming simulations for 0°/90° biaxial non-crimp fabrics. Mater Res Proc 2025;54:554–63. http://dx.doi.org/10.21741/9781644903599-60.

[72] Schäfer B, Zheng R, Naouar N, Kärger L. Membrane behavior of uni- and bidirectional non-crimp fabrics in off-axis-tension tests. Int J Mater Form 2023;16(6):68. http://dx.doi.org/10.1007/s12289-023-01792-x.

[73] Boisse P, Hamila N, Guzman-Maldonado E, Madeo A, Hivet G, dell'Isola F. The bias-extension test for the analysis of in-plane shear properties of textile composite reinforcements and prepregs: a review. Int J Mater Form 2016;10(4):473–92. http://dx.doi.org/10.1007/s12289-016-1294-7.

[74] Schäfer B, Dörr D, Zheng R, Naouar N, Kärger L. A hyperelastic approach for modeling the membrane behavior in finite element forming simulation of unidirectional non-crimp fabrics (UD-NCF). Compos Part A: Appl Sci Manuf 2024;185:108359. http://dx.doi.org/10.1016/j.compositesa.2024.108359.

[75] ten Thije R, Akkerman R. Solutions to intra-ply shear locking in finite element analyses of fibre reinforced materials. Compos Part A: Appl Sci Manuf 2008;39(7):1167–76. http://dx.doi.org/10.1016/j.compositesa.2008.03.014.

[76] Hamila N, Boisse P. Locking in simulation of composite reinforcement deformations. analysis and treatment. Compos Part A: Appl Sci Manuf 2013;53:109–17. http://dx.doi.org/10.1016/j.compositesa.2013.06.001.

[77] Hamila N, Boisse P. Tension locking in finite-element analyses of textile composite reinforcement deformation. C R Mécanique 2013;341(6):508–19. http://dx.doi.org/10.1016/j.crme.2013.03.001.

[78] Schäfer B, Zheng R, Boisse P, Kärger L. Investigation of the compaction behavior of uni- and bidirectional non-crimp fabrics. Mater Res Proc 2023;28:331–8. http://dx.doi.org/10.21741/9781644902479-36.

[79] Robitaille F, Gauvin R. Compaction of textile reinforcements for composites manufacturing. I: Review of experimental results. Polym Compos 1998;19(2):198–216. http://dx.doi.org/10.1002/pc.10091.

[80] Mitsch J, Schäfer B, Kärger L. Significance of the material parameters within a three-dimensional solid-shell element for thermoforming simulation. Mater Res Proc 2025;54:363–72. http://dx.doi.org/10.21741/9781644903599-40.

[81] Broberg PH, Lindgaard E, Krogh C, Jensen SM, Trabal GG, Thai A-M, et al. One-click bending stiffness: Robust and reliable automatic calculation of moment–curvature relation in a cantilever bending test. Compos Part B: Eng 2023;39(9):110763. http://dx.doi.org/10.1016/j.compositesb.2023.110763.

[82] Schäfer B, Naouar N, Kärger L. Investigation of the friction behavior of uni- and bidirectional non-crimp fabrics. Mater Res Proc 2024;41:540–8. http://dx.doi.org/10.21741/9781644903131-60.

[83] Schäfer B, Zheng R, Colmars J, Platzer A, Naouar N, Boisse P, et al. Experimental analysis of the forming behavior of uni- and bidirectional non-crimp fabrics for different geometries. Compos Part B: Eng 2024;287:111765. http://dx.doi.org/10.1016/j.compositesb.2024.111765.

[84] Jiao W, Chen L, Xie J, Yang Z, Guo Z. Deformation mechanisms of 3D LTL woven preforms in hemisphere forming tests. Compos Struct 2022;283:115156. http://dx.doi.org/10.1016/j.compstruct.2021.115156.

[85] Bai R, Colmars J, Chen B, Naouar N, Boisse P. The fibrous shell approach for the simulation of composite draping with a relevant orientation of the normals. Compos Struct 2022;285(8):115202. http://dx.doi.org/10.1016/j.compstruct.2022.115202.

[86] Kärger L, Galkin S, Zimmerling C, Dörr D, Linden J, Oeckerath A, et al. Forming optimisation embedded in a CAE chain to assess and enhance the structural performance of composite components. Compos Struct 2018;192:143–52. http://dx.doi.org/10.1016/j.compstruct.2018.02.041.

[87] Schäfer F, Werner HO, Henning F, Kärger L. A hyperelastic material model considering biaxial coupling of tension–compression and shear for the forming simulation of woven fabrics. Compos Part A: Appl Sci Manuf 2023;165(4):107323. http://dx.doi.org/10.1016/j.compositesa.2022.107323.

[88] Lomov SV, Barburski M, Stoilova T, Verpoest I, Akkerman R, Loendersloot R, et al. Carbon composites based on multiaxial multiply stitched preforms. Part 3: Biaxial tension, picture frame and compression tests of the preforms. Compos Part A: Appl Sci Manuf 2005;36(9):1188–206. http://dx.doi.org/10.1016/j.compositesa.2005.01.015.